

Ionospheric energy input in response to changes in solar wind driving: Statistics from the SuperDARN and AMPERE campaigns

Daniel D Billett¹, Kathryn A McWilliams¹, Gareth William Perry², Lasse Boy Novock Clausen³, and Brian J. Anderson⁴

¹University of Saskatchewan

²New Jersey Institute of Technology

³University of Oslo

⁴John Hopkins Univ.

November 24, 2022

Abstract

For over a decade, the Super Dual Auroral Radar Network (SuperDARN) and the Active Magnetosphere and Planetary Electrodynamics Response Experiment (AMPERE) have been measuring ionospheric convection and field-aligned currents in the high-latitude regions, respectively. Using both, whole hemisphere maps of the magnetosphere-ionosphere energy transfer rate (the Poynting flux) have been generated with a time resolution of two minutes between 2010 and 2017. These uniquely data driven Poynting flux patterns are used in this study to perform a superposed epoch analysis of the northern hemisphere ionospheric response to transitions of the IMF B_z component. We discuss the difference in the distribution of Poynting flux between the magnetosphere-ionosphere Dungey cycle “switching on” and “switching off” to solar wind driving, revealing that they are not symmetric temporally or spatially.

1 **Ionospheric energy input in response to changes in**
2 **solar wind driving: Statistics from the SuperDARN**
3 **and AMPERE campaigns**

4 **D. D. Billett¹, K. A. McWilliams¹, G. W. Perry², L. B. N. Clausen³, B. J.**
5 **Anderson⁴**

6 ¹Institute of Space and Atmospheric Studies, University of Saskatchewan, Saskatoon, SK, Canada

7 ²Center for Solar-Terrestrial Research, New Jersey Institute of Technology, Newark, NJ, USA

8 ³Department of Physics, University of Oslo, Oslo, Norway

9 ⁴Applied Physics Laboratory, Johns Hopkins University, Laurel, Maryland, USA

10 **Key Points:**

- 11 • SuperDARN and AMPERE derived Poynting flux distributions are generated with
12 a two-minute resolution.
- 13 • A superposed epoch analysis is performed for transitions of the IMF B_z compo-
14 nent.
- 15 • There is spatial and temporal asymmetry to how the Poynting flux morphology
16 responds to opposite B_z transitions.

Abstract

For over a decade, the Super Dual Auroral Radar Network (SuperDARN) and the Active Magnetosphere and Planetary Electrodynamics Response Experiment (AMPERE) have been measuring ionospheric convection and field-aligned currents in the high-latitude regions, respectively. Using both, whole hemisphere maps of the magnetosphere-ionosphere energy transfer rate (the Poynting flux) have been generated with a time resolution of two minutes between 2010 and 2017. These uniquely data driven Poynting flux patterns are used in this study to perform a superposed epoch analysis of the northern hemisphere ionospheric response to transitions of the IMF B_z component. We discuss the difference in the distribution of Poynting flux between the magnetosphere-ionosphere Dungey cycle “switching on” and “switching off” to solar wind driving, revealing that they are not symmetric temporally or spatially.

Plain Language Summary

The Earth’s high-latitude upper atmosphere (the ionosphere, upwards of 100km in altitude) is consistently bombarded with solar energy that takes the form of electric currents aligned with Earth’s magnetic field. The magnetosphere has two generalised states, “open” and “closed”. Open is when the Earth and solar magnetic fields connect to each other on the dayside, allowing energy into the atmosphere from the solar wind. Closed is when the fields do not connect (or do not connect simply) and thus not as much energy enters the atmosphere. The open or closed criteria depends on the direction of the solar magnetic field, which varies constantly. In this study, we utilise nearly 8 years of data to generate average patterns of ionospheric energy input at various intervals before and after the solar-magnetosphere system transitions from open to closed, and vice versa. We discuss the spatial and temporal timescales upon which the energy varies in response to the relatively symmetric transitions, finding that they do not result in symmetric changes in the ionospheric energy input patterns.

1 Introduction

In 2009, the Iridium constellation of satellites began consistently delivering magnetic field data at their orbital altitude of ~ 780 km to be processed as part of the Active Magnetosphere and Planetary Electrodynamics Response Experiment (AMPERE; Anderson et al., 2014). AMPERE has allowed for the derivation of global-scale pertur-

48 bation magnetic fields at F-region ionospheric altitudes (at a typical 10-minute resolu-
 49 tion), which are subsequently processed into patterns of the high-latitude field-aligned
 50 currents (FACs). Overlapping with the entirety of the AMPERE dataset from its incep-
 51 tion to the present day has been consistent measurements of ionospheric plasma flows
 52 from the Super Dual Auroral Radar Network (SuperDARN; Greenwald et al., 1995). As
 53 of 2021, the SuperDARN consists of 36 high-frequency radars in both the northern and
 54 southern hemispheres that are used conjunctively to generate instantaneous patterns of
 55 the high-latitude ionospheric convection pattern (Chisham et al., 2007; Nishitani et al.,
 56 2019), at a two-minute resolution.

57 SuperDARN derived convection, or electric potential (Φ), patterns can be converted
 58 to the electric field (\mathbf{E}) via the relation $\mathbf{E} = -\nabla\Phi$. AMPERE derived perturbation mag-
 59 netic fields ($\delta\mathbf{B}$), based on the assumption that the magnetic field is near-vertical at high
 60 latitudes, can then be used in conjunction with \mathbf{E} to calculate the total energy trans-
 61 ferred between the magnetosphere and ionosphere through field aligned currents (FACs),
 62 the Poynting flux (\mathbf{S}_{\parallel}), using Poynting’s theorem:

$$63 \quad \mathbf{S}_{\parallel} = -\frac{1}{\mu_0} (\mathbf{E} \times \delta\mathbf{B}) \cdot \hat{\mathbf{r}} \quad (1)$$

64 where $\hat{\mathbf{r}}$ is the unit vector parallel to the geomagnetic field and μ_0 is the permeability
 65 of free space. Previously, a dataset of Poynting flux patterns for the northern hemisphere
 66 ionosphere has been generated for the entire overlapping AMPERE-SuperDARN datasets
 67 between 2010 and 2017 using Equation 1, which have been shown to be consistent with
 68 several models and observations (Billett et al., 2021).

69 This study utilises the new dataset of northern hemisphere Poynting flux maps to
 70 examine its statistical response to changes in solar wind driving conditions, primarily
 71 after sustained transitions of the Interplanetary Magnetic Field (IMF) B_z component
 72 in Geocentric Solar Magnetospheric (GSM) coordinates. These types of IMF transitions
 73 are akin to “switching on” ($B_z > 0$ to $B_z < 0$) and “switching off” ($B_z < 0$ to $B_z >$
 74 0) magnetospheric driving of the ionosphere via reconnection at the magnetopause, in-
 75 ducing the Earth’s Dungey cycle (Dungey, 1961; Cowley & Lockwood, 1992). Although
 76 this is a simplistic view of magnetosphere-ionosphere coupling given that magnetopause
 77 reconnection can still occur at the magnetopause when the IMF B_z is positive (Onsager
 78 et al., 2001), whether the IMF vector is southward ($B_z < 0$) or northward ($B_z > 0$)

orientated is the most significant indicator of magnetospheric energy input into the ionosphere (Milan, 2009).

The “switching on” of the magnetosphere-ionosphere driving system (i.e., a positive-to-negative IMF B_z transition) has been extensively studied. For example, the ionospheric electric field is known to respond dynamically to changes in the near-Earth solar wind on the order of minutes (e.g. Murr & Hughes, 2001; Yu & Ridley, 2009; Snekvik et al., 2017). This response begins on the dayside and progresses to the nightside, with the ionospheric electric field fully reconfiguring to a negative B_z orientation within tens of minutes (e.g. Murr & Hughes, 2001; Dods et al., 2017). The global FACs system finish developing much later, on the order of hours (Coxon et al., 2019). Ionospheric conductivity is also known to play an important role in the rate of FAC formation, contributing to seasonal asymmetries (Coxon et al., 2016).

Negative to positive turnings of the IMF B_z have less commonly been studied. Lobe reconnection under positive B_z results in the development of a new FAC system (NBZ; Iijima et al., 1984), thus lowering the decay rate of the total dayside current and bringing it more in line with the total nightside current decay (Milan et al., 2018). Decay rates are further complicated by the different responses of reconnection driven magnetospheric convection and viscous interaction or flywheel driven convection under positive B_z (Bhattarai et al., 2012). Low nightside conductance may in fact result in faster nightside FAC decay due to weaker line-tying of magnetic field lines (Moretto et al., 2018, 2021).

In this paper, we present the response of the northern hemispheric Poynting flux to the aforementioned B_z transitions as a superposed epoch analysis. We discuss how the overlapping SuperDARN and AMPERE data sets were used to do this in section 2. Results are shown in section 3, whilst we discuss the differences in how Poynting flux increases or decreases depending on the B_z transition in section 4.

2 Data processing

Maps of the high-latitude Poynting flux were generated for each overlapping AMPERE $\delta\mathbf{B}$ map and SuperDARN convection pattern in the northern hemisphere using the method described by Waters et al. (2004). In short, both $\delta\mathbf{B}$ from AMPERE and \mathbf{E} from the SuperDARN are placed into an equal area ($\sim 200 \times 400$ km) grid poleward of 60° AACGM (Shepherd, 2014) latitude which is also fixed in local time, where each cell

110 is 2° of latitude tall. Equation 1 is then used to derive the Poynting flux on the same
111 grid. All latitudes and magnetic local times (MLTs) mentioned henceforth are referring
112 to AACGM latitude and local time, respectively.

113 As the global SuperDARN convection patterns are spherical harmonic fits to the
114 plasma velocity data from individual radars (Ruohoniemi & Baker, 1998), a threshold
115 of 200 gridded SuperDARN line-of-sight velocity data points per pattern is imposed be-
116 fore using them to calculate the Poynting flux. This ensures there is generally a good
117 spread of real radar velocity data across most local times for any given convection map
118 and reduces the amount of “usable” SuperDARN convection patterns for Poynting flux
119 measurements by around 55% (Billett et al., 2018). The SuperDARN radar data is also
120 filtered so that E-region ionospheric backscatter is removed, giving the convection pat-
121 terns an assumed F-region altitude of approximately 250 km. Convection patterns use
122 SuperDARN data integrated over two minutes.

123 The AMPERE data is assumed to be from an altitude of 780 km, which is subse-
124 quently scaled to an altitude of 250 km to match the SuperDARN data. This is done us-
125 ing the $3/2$ relationship described by Knipp et al. (2014) and results in $\delta\mathbf{B}$ being approx-
126 imately 1.12 times larger than measured. $\delta\mathbf{B}$ maps have a two-minute resolution and a
127 sliding 10-minute integration window, so when combined with SuperDARN data, Poynt-
128 ing flux maps are calculated at a two-minutes resolution.

129 In this study, a superposed epoch analysis of the Poynting flux with an epoch spac-
130 ing of two minutes was carried out for sustained transitions of the IMF B_z component.
131 IMF data is obtained from the 1-minute resolution OMNI dataset (retrieved from [http://](http://omniweb.gsfc.nasa.gov)
132 omniweb.gsfc.nasa.gov) and is time shifted forward by 10 minutes to account for the
133 travel between the magnetopause and ionosphere. “Sustained” transitions are defined
134 as intervals where B_z was constantly northward (southward) orientated for at least 30
135 minutes prior to becoming southward (northward), upon which the sign of B_z remained
136 the same for an additional 30 minutes. Using 30 minutes prior to the transition allows
137 time for the ionosphere to be “settled” under the initial negative or positive B_z by epoch
138 t_0 . 30 minutes after the transition gives a window to examine the Poynting flux response
139 to the IMF change, which is long enough for the ionospheric electric field to converge to
140 state equivalent to statistical patterns on average (Grocott & Milan, 2014). In order to

141 maintain a high number of Poynting flux maps for averaging, no B_z magnitude thresh-
 142 old was imposed and the IMF B_y component was not considered.

143 **3 Results**

144 The results of the Poynting flux superposed epoch analysis, for sustained north-
 145 to-south and south-to-north IMF B_z transitions, are shown in Figure 1. There were 1301
 146 north-to-south and 1307 south-to-north transitions during the SuperDARN-AMPERE
 147 overlap period, but only Poynting flux maps which met the 200 SuperDARN data point
 148 threshold were used in the average for each epoch (the total in each denoted by the num-
 149 ber in the top left of the sub-plots). There was no transition bias towards a specific year,
 150 season, sign of B_y or magnitude of B_z .

151 The patterns shown in Figure 1 are from 4 minutes prior to the IMF transition to
 152 30 minutes after in two-minute intervals. Epochs prior to $t_0 - 4$ are not shown here as
 153 they do not vary significantly from $t_0 - 4$. Only positive (downward) Poynting fluxes are
 154 shown, as negative (upward) values are nearly always small, thus averaging out. This
 155 is to be expected because the ionosphere is on average a passive load to the magneto-
 156 sphere, not vice versa. We note that more Poynting maps meet the 200 SuperDARN data
 157 point criteria when the IMF is southward, signifying the SuperDARN radars receiving
 158 more ionospheric backscatter during more geomagnetically active periods.

159 For the north-to-south transition in Figure 1a, there are regions of enhanced down-
 160 ward Poynting flux (PF) that are consistent in their morphology throughout all epochs.
 161 These are lower latitude enhancements around 70° latitude on both the dawn and dusk
 162 sides, as well as a higher latitude enhancement around 80° latitude centred slightly duskward
 163 of noon MLT. Before t_0 , the highest PF magnitude is in the high-latitude dayside region.
 164 From t_0 to t_0+30 , PF gradually increases starting at dayside local times and eventually
 165 affecting nightside local times. The largest PF magnitudes at t_0+30 are located around
 166 80° latitude centred on noon MLT, as well as around 70° latitude in the 05-09 and 13-
 167 18 MLT regions. PF is noticeably smaller for nightside local times, and non-existent near
 168 midnight for all latitudes. There is a gradual movement of dawn and duskside enhanced
 169 PF equatorward between t_0 and t_0+30 .

170 In Figure 1b, the IMF B_z south-to-north transition of downward Poynting flux is
 171 shown. Before t_0 , the magnitudes are similar to that in the t_0+30 epoch of the northward-

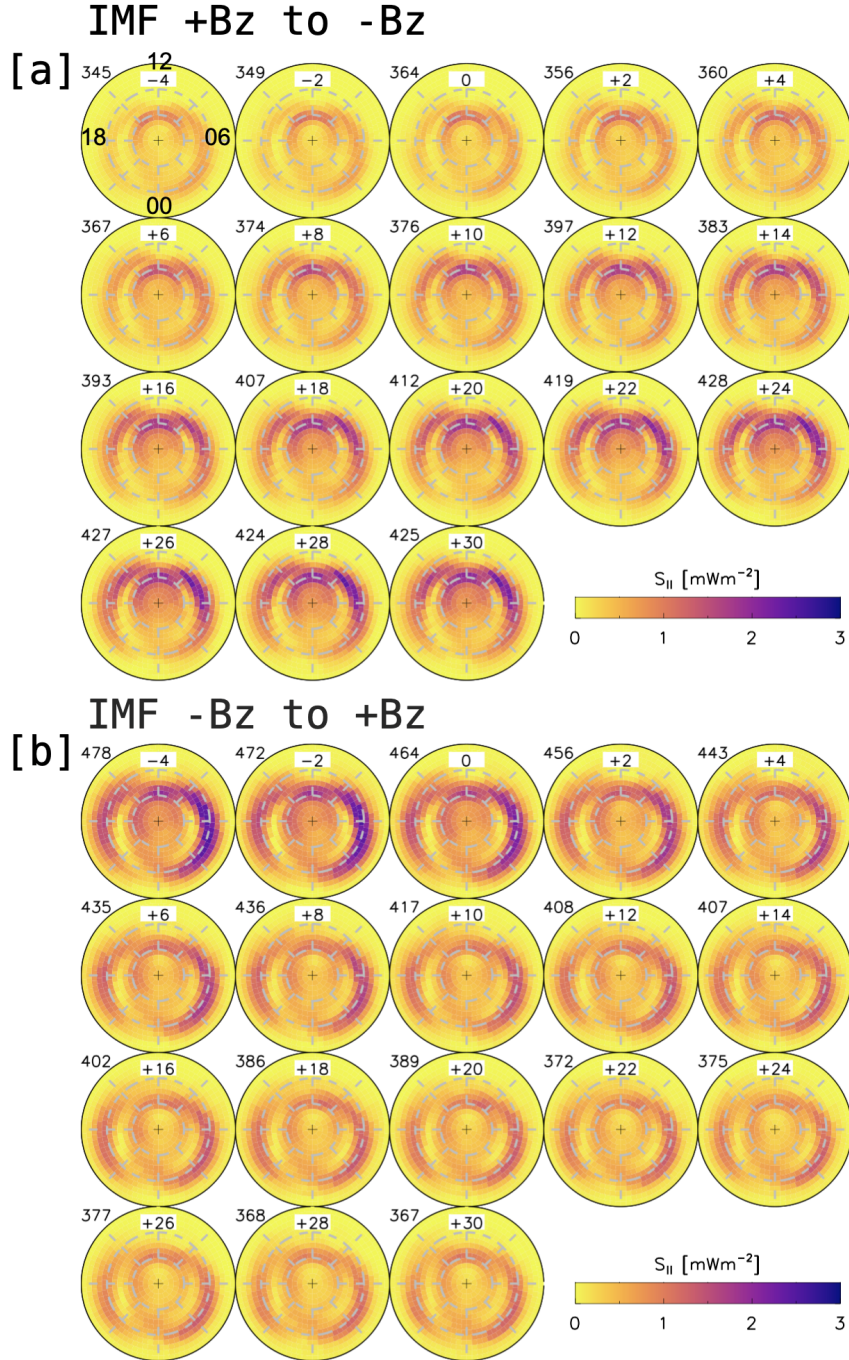


Figure 1. Superposed epoch maps of the downward Poynting flux from $t_0 - 4$ to $t_0 + 30$, for [a] northward-to-southward and [b] southward-to-northward IMF B_z transitions. Plots are polar projections in AACGM latitude and local time. Noon is to the top and dawn is to the right of each plot. Concentric circles separate 10° of latitude, down to a 60° minimum. Numbers in the top left of each plot denote the number of averages in each epoch.

172 to-southward transition shown in 1a, but the enhanced dawnside PF extends significantly
 173 closer to midnight MLT. At +2 minutes, there appears to be a steep decrease in PF mag-
 174 nitude when compared to t_0 , which is particularly evident in the high-latitude dayside
 175 and lower latitude dawnside regions. A similar sharp change after t_0 does not seem to
 176 be present for the B_z northward-to-southward transition in Figure 1a. At t_0+30 in Fig-
 177 ure 1b, the PF is decreased at all local times from t_0 .

178 To further examine the changes in downward Poynting flux magnitudes after the
 179 IMF B_z transitions, Figure 2 shows sets of time series plots from 30 minutes prior to 30
 180 minutes after a transition. The data has been averaged over four local time sectors 6 hours
 181 in width each: the nightside (21-03 MLT, red diamonds), dawnside (03-09 MLT, blue squares),
 182 dayside (09-15 MLT, yellow circles) and duskside (15-21 MLT, green triangles). The time
 183 series have also been area integrated both below and above 75° latitude to differentiate
 184 between Poynting flux variations in the lower and higher latitude regions identified pre-
 185 viously. The result is the total inbound power for 8 sectors, which we refer to as Poynt-
 186 ing flux power (PFP).

187 Figure 2a shows the B_z north-to-south transition for the lower latitude ($<75^\circ$) re-
 188 gion. Prior to t_0 , dawnside and nightside PFP is the largest (~ 0.3 GW), followed by dusk-
 189 side (~ 0.25 GW) and dayside (<0.05 GW). Dawn and duskside PFP increase after t_0 at
 190 a steady rate, to 0.9 and 0.8 GW respectively at t_0+30 , with duskside PFP overtaking
 191 the magnitude of nightside PFP. Dayside PFP increases to 0.2 GW after t_0 , whilst night-
 192 side PFP changes very little.

193 For the higher latitude ($<75^\circ$) B_z north-to-south transition (Figure 2b), all regions
 194 average a PFP between 0.2 and 0.4 GW before t_0 . Dayside PFP is largest and under-
 195 goes the most significant increase between t_0 and t_0+30 , up to ~ 1.1 GW. Dawn and
 196 duskside PFP remain comparable as they increase to 0.7 GW, while nightside PFP in-
 197 creases very gradually to 0.35 GW.

198 In Figure 2c, the B_z south-to-north transition for the lower latitude region is shown.
 199 From before t_0 to t_0+30 , dawnside PFP decreases from 1.4 to 0.6 GW, duskside from
 200 1.05 to 0.5 GW, nightside from 0.6 to 0.5 GW and dayside from 0.35 to 0.1 GW. We note
 201 that the PFP magnitudes at the beginning (t_0-30) of the epoch analysis, in particular
 202 on the dawn and dusk sides, are larger than corresponding magnitudes at t_0+30 in fig-
 203 ure 2a (i.e., the reverse B_z transition). This implies that 30 minutes is not long enough

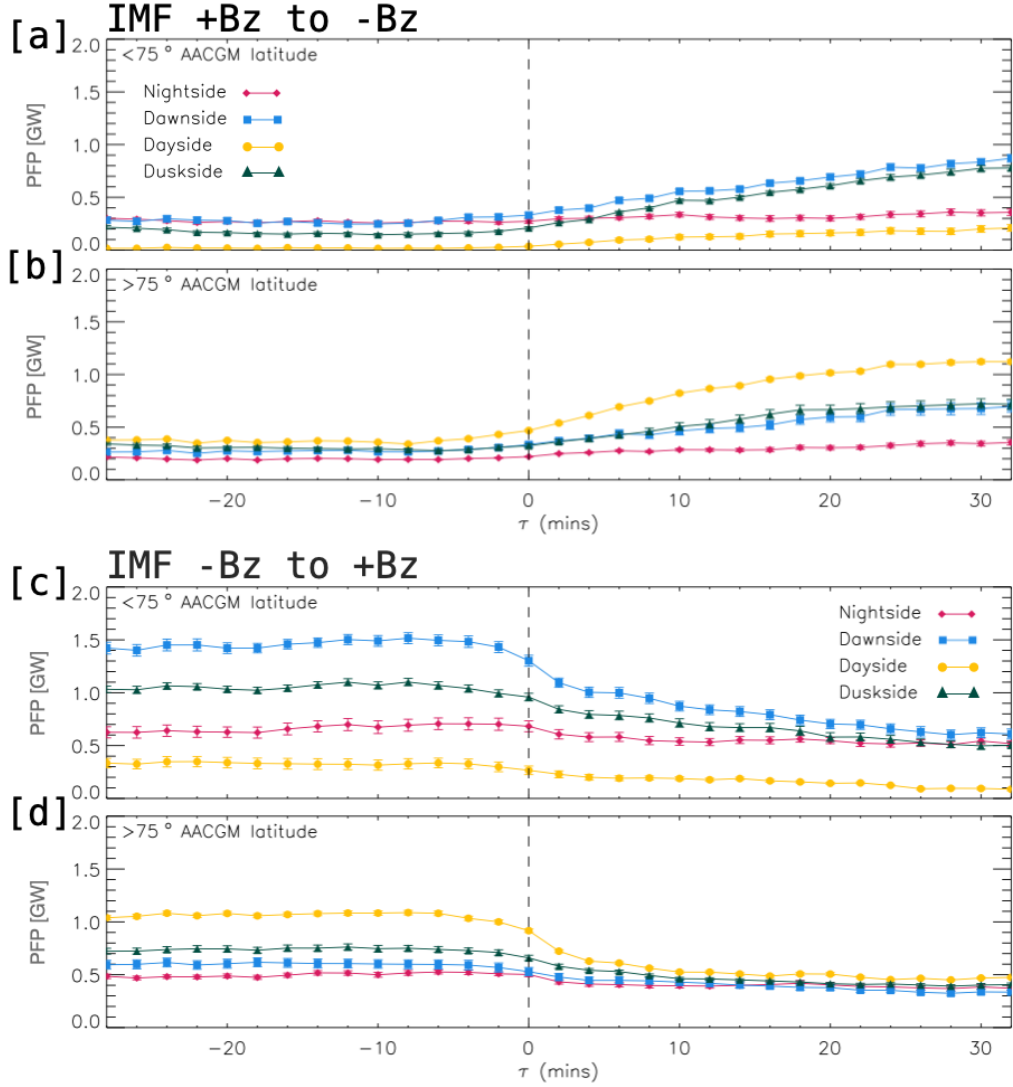


Figure 2. Superposed epoch time series of the downward Poynting flux averaged over night-side, dawnside, dayside and duskside local times. [a] and [b]: northward-to-southward transitions. [c] and [d]: southward-to-northward transitions. Averages are also split into below ([a] and [c]) and above ([b] and [d]) 75° latitude. Standard errors are also shown, but are often smaller than the plotting symbols used.

204 for the Poynting flux magnitude to stabilise to the new IMF orientation, which will be
 205 commented on further in the discussion section.

206 Dayside PFP is dominant at high latitudes for the B_z south-to-north transition (Fig-
 207 ure 2d), dropping from 1.05 before t_0 to 0.5 GW at t_0+30 . Duskside, dawnside and night-
 208 side PFP have lower initial magnitudes of 0.7, 0.6 and 0.5 GW respectively, all decreas-

209 ing to $\sim 0.35\text{-}0.4$ GW. We note that for south-to-north B_z transitions (both Figure 2d
 210 and e), the initial PFP decrease after t_0 appears sharper at all local times than the cor-
 211 responding increase in the north-to-south transition (Figure 2a and b).

212 From Figure 2, it is evident that different local times and latitudinal regions respond
 213 at different rates to an IMF B_z transition. In Figure 3, maps of the Poynting flux per-
 214 centage increase (for B_z north-to-south transitions, [a]) and percentage decrease (for south-
 215 to-north transitions, [b]) from t_0 are shown. Epochs shown are from t_0+2 minutes to t_0+30
 216 minutes. Only the percentage increase or decrease is shown for respective transitions be-
 217 cause on average, the Poynting flux does not decrease for B_z north-to-south transitions
 218 and vice versa. This is not strictly true for single events and localised regions where very
 219 small PF fluctuations can occur in both the positive and negative direction, irregardless
 220 of B_z transition. Small localised fluctuations, defined as a <0.1 mWm^{-2} increase or de-
 221 crease from t_0 , are however removed from Figure 3. Figure 3 is not to illustrate the mag-
 222 nitude of Poynting flux changes in certain regions, but more as an indication of the rate
 223 of Poynting flux change normalised by initial magnitudes at t_0

224 In Figure 3a, large percentage enhancements of the Poynting flux (+100% or more)
 225 within 10 minutes of the B_z north-to-south transition occur on the dayside and prop-
 226 agate towards the nightside, mainly between $65\text{-}75^\circ$ latitude and near the pole. In par-
 227 ticular, the post-noon sector PF appears to increase the fastest. The nightside propa-
 228 gation continues with increasing epoch up to 30 minutes after the transition, where per-
 229 centage increases from t_0 reach nearly +400% on the dayside in the post- and pre-noon
 230 sectors. There is a clear gradual expansion of the enhancement regions equatorward with
 231 increasing epoch, particularly on the nightside a few hours pre- and post-midnight, where
 232 there are large percentage enhancements near 60° latitude at t_0+30 .

233 Within 10 minutes of a B_z south-to-north transition (Figure 3b), Poynting flux per-
 234 centage decreases of several tens of percent appear to occur both on the day and night-
 235 side simultaneously. This initial decrease occurs across most local times and is roughly
 236 confined to near the pole (particularly on the dayside), as well as between $65\text{-}75^\circ$ lat-
 237 itude on the dawn and dusk sides. PF continues to decrease on the dawn and dusk sides
 238 with increasing epoch, decreasing first at lower latitudes and then later at higher lati-
 239 tudes. By t_0+30 , PF decreases by as much as 80% at lower latitudes on the dawn and
 240 dusk sides have occurred.

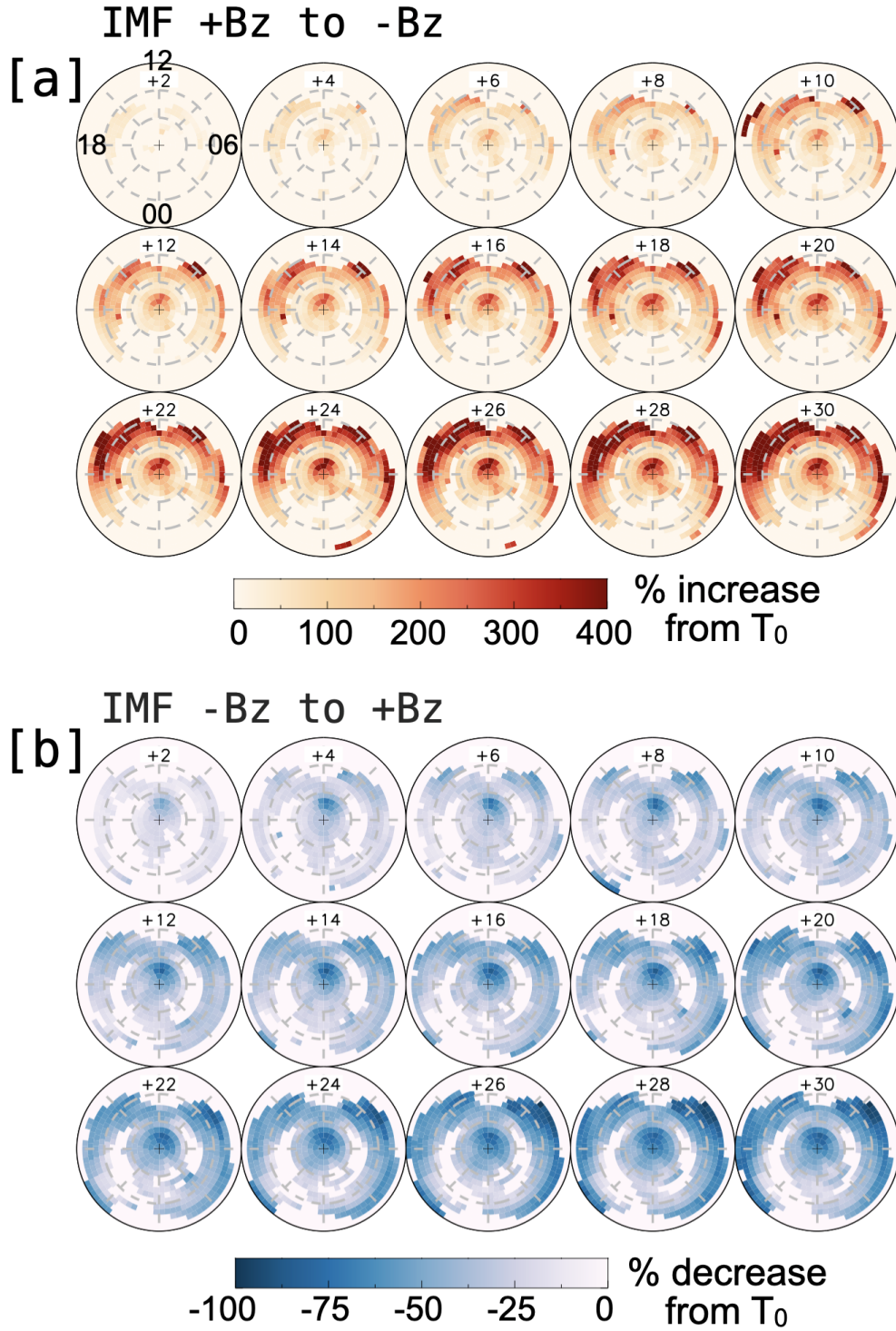


Figure 3. Poynting flux percentage change maps from epoch t_0 . [a]: Percentage increase after northward-to-southward transitions. [b]: Percentage decrease after southward-to-northward transitions.

4 Discussion

The superposed epoch analysis presented in this study has shown the reconfiguration process of high-latitude Poynting flux in response to sign transitions of the IMF B_z component, with a two-minute temporal resolution and a spatial resolution of a few hundred kilometres. The Poynting flux patterns shown in this study have a similar general morphology to those in previous studies of Poynting Flux/Joule heating (e.g. Weimer, 2005; Cosgrove et al., 2014) as well as the initial manuscript that introduces this data set (Billett et al., 2021). In short, Poynting flux is mostly dissipated at the auroral electrojets where R1/R2 FACs close on the dawn/dusk sides, as well as around the day-side cusp at $\sim 80^\circ$ latitude. Many previous authors have noted that the high-latitude ionosphere responds almost instantly to IMF changes (e.g. Murr & Hughes, 2001), and we too observe a very fast (< 2 minute) response of the Poynting flux for both north-to-south and south-to-north B_z transitions. The differences between the magnitude of Poynting flux before a transition and 30 minutes after are drastic, but the timescales of which changes occur in local time are gradual and not symmetric for opposite B_z transitions.

We have found that 30 minutes is not long enough for the morphology of Poynting flux to fully reconfigure after an IMF transition, but is long enough to reveal significant asymmetries between the two transitions types shown here. Figure 2a and d for example shows that PFP in the low latitude dawn and dusk sectors do not totally converge to pre-transition magnitudes of the opposite transition. The full Poynting flux reconfiguration timescale is thus consistent with FAC reconfiguration timescales reported by previous authors (e.g. Anderson et al., 2018; Coxon et al., 2019). Our results are also in agreement with Moretto et al. (2021), in that most of the Poynting flux reconfigures within 30 minutes following a B_z transition. The high-latitude dayside region, the area dominated by Poynting flux into the cusp, conversely appears to completely reconfigure within 30 minutes of a B_z transition. As the cusp region is typically close to the boundary between open and closed (to the solar wind) geomagnetic field lines, the shorter reconfiguration time is perhaps not surprising.

For both B_z transitions, there is a region close to the pole on the dayside that experiences a large percentage increase or decrease in downward Poynting flux (Figure 3). This region is on newly opened field lines following a southward transition, and connected to the magnetospheric lobes following a northward transition. The Poynting flux mag-

273 nitude is not particularly large near the pole compared to the main regions of enhance-
274 ment, but the change that occurs there is drastic probably because the electric field rapidly
275 changes in response to IMF orientation fluctuations. During southward IMF for exam-
276 ple, \mathbf{E} is strongly duskward near the pole (i.e. anti-sunward convection) and starts de-
277 creasing within a few minutes following a northward turning (Knipp et al., 1991). The
278 opposite also occurs quickly for the north-to-south transition.

279 Evident in our analysis is the expanding-contracting polar cap (Cowley & Lock-
280 wood, 1992). After IMF B_z north-to-south transitions for example, we can clearly see
281 an immediate increase of the dayside downward Poynting flux, followed by increases at
282 local times gradually approaching nightside local times (Figure 3a). This is in agreement
283 with magnetopause reconnection transferring flux into the polar cap and causing it to
284 expand, activating R1 and R2 field aligned currents on the dayside. Anderson et al. (2018)
285 noted that night side FAC activation was lagged approximately 30 minutes after the on-
286 set of dayside currents, caused by the release of magnetic flux build up in the magne-
287 totail, which would explain why Poynting flux increases appear heavily dayside domi-
288 nant for the first 30 minutes following a B_z north-to-south transition. A future study
289 in this area could focus on Poynting flux changes later than 30 minutes post IMF tran-
290 sition, examining in more depth the dayside-to-nightside morphology changes.

291 A perhaps surprising result is that for B_z south-to-north transitions, the decrease
292 of Poynting flux at both dayside and nightside local times seem relatively symmetric (Fig-
293 ure 3b), with perhaps a slightly faster decrease on the dayside. It would perhaps be ex-
294 pected that the sudden ending of magnetopause reconnection would cause dayside Poynt-
295 ing flux to decrease whilst nightside reconnection lingers, causing a lagged nightside re-
296 sponse (in line with the ~ 30 -minute reconfiguration times of the ionospheric electric field;
297 Grocott & Milan, 2014). As this is not the case, the relatively symmetric decrease of Poynt-
298 ing flux at most local times could be due to the neutral wind flywheel effect maintain-
299 ing the ionospheric electric field. That is, after the winds were previously enhanced by
300 ion-neutral collisions (whilst the ionosphere was being actively driven by magnetopause
301 reconnection), they maintained ionospheric plasma circulation when the IMF turned north-
302 ward (e.g. Deng et al., 1991).

303 In addition to the ionospheric electric field, the Poynting flux is also controlled by
304 magnetic perturbations from FACs. The role of the ionospheric Pedersen conductance

305 plays an important role in the generation and decay of FACs, thus impacting the decay
 306 of Poynting flux after the south-to-north B_z transition. A higher conductance can re-
 307 sult in slower FAC formation or decay (Moretto et al., 2021), so the lower conductance
 308 of the nightside compared to the dayside would result in faster nightside FAC decay. Im-
 309 mediately after a northward transition of B_z however, following the extended period of
 310 southward B_z , substorms and the auroral oval may still be active and thus contribute
 311 to higher conductance in the nightside auroral zones. Additionally, on the dayside, the
 312 generation of NBZ currents following a northward IMF transition impede dayside FAC
 313 decay (Milan et al., 2018). After a B_z northward transition, there must be a complicated
 314 balance between conductance at various dayside and nightside local times for the Poynt-
 315 ing flux to decrease roughly at the same rate.

316 5 Summary

317 In summary, we have performed a superposed epoch analysis of the high-latitude
 318 northern hemisphere Poynting flux to changes in the IMF B_z component. The analy-
 319 sis was carried out using ~ 7.5 years of overlapping SuperDARN and AMPERE data at
 320 a 2-minute resolution, allowing for a data driven look at how the magnitude and mor-
 321 phology of Poynting flux changes when the Dungey cycle is switched “on” or “off”. Our
 322 key results are that:

- 323 • B_z positive-to-negative and negative-to-positive transitions are not symmetric in
 324 how Poynting flux increases or decreases. For positive-to-negative, there is a clear
 325 dayside-to-nightside progression of the increasing Poynting flux. For negative-to-
 326 positive transitions, Poynting flux decreases simultaneously at most local times,
 327 with dayside Poynting flux decreasing only slightly faster than that on the night-
 328 side.
- 329 • Total reconfiguration times of the Poynting flux morphology and magnitudes are
 330 longer than 30 minutes, except in the high-latitude cusp region where it is roughly
 331 30 minutes.

332 It is likely that there is a complicated interplay between ionospheric conductance
 333 on the dayside and nightside, which is affecting Poynting flux decay rates for B_z negative-
 334 to-positive transitions and resulting in the near simultaneous decrease at most local times.
 335 For example, lingering auroral activity on the nightside or the formation of NBZ cur-

336 rents on the dayside could be lengthening or shortening field-aligned current decay rates
 337 respectively. There is also a potential impact from thermospheric winds, as they could
 338 maintain the ionospheric electric field after northward B_z turnings due to the flywheel
 339 effect.

340 Acknowledgments

341 This research was supported by the National Sciences and Engineering Research Coun-
 342 cil of Canada (NSERC). DDB was supported by NSERC CREATE Grant #479771-20,
 343 whilst KM was supported by NSERC Discovery Grant #RGPIN 05472-2017. The au-
 344 thors acknowledge the use of data from SuperDARN, an international project made pos-
 345 sible by the national funding agencies of Australia, Canada, China, France, Italy, Japan,
 346 South Africa, Norway, the United Kingdom and the United States of America. Super-
 347 DARN data can be downloaded from Globus, instructions of which are provided here:
 348 <https://superdarn.ca/data-products>. SuperDARN data in this study was processed
 349 using the Radar Software Toolkit (RST), version 4.5: [https://doi.org/10.5281/zenodo](https://doi.org/10.5281/zenodo.4435297)
 350 [.4435297](https://doi.org/10.5281/zenodo.4435297). We also thank the AMPERE team and the AMPERE Science Center for pro-
 351 viding the Iridium derived data products, which can be plotted and downloaded at: [http://](http://ampere.jhuapl.edu/)
 352 ampere.jhuapl.edu/.

353 References

- 354 Anderson, B. J., Korth, H., Waters, C. L., Green, D. L., Merkin, V. G., Barnes,
 355 R. J., & Dyrud, L. P. (2014). Development of large-scale Birkeland currents
 356 determined from the Active Magnetosphere and Planetary Electrodynamic
 357 Response Experiment. *Geophysical Research Letters*, *41*(9), 3017–3025.
- 358 Anderson, B. J., Olson, C. N., Korth, H., Barnes, R. J., Waters, C. L., & Vines,
 359 S. K. (2018). Temporal and spatial development of global Birkeland currents.
 360 *Journal of Geophysical Research: Space Physics*, *123*(6), 4785–4808.
- 361 Bhattarai, S. K., Lopez, R. E., Bruntz, R., Lyon, J. G., & Wiltberger, M. (2012).
 362 Simulation of the polar cap potential during periods with northward inter-
 363 planetary magnetic field. *Journal of Geophysical Research: Space Physics*,
 364 *117*(A4).
- 365 Billett, D. D., Grocott, A., Wild, J. A., Walach, M.-T., & Kosch, M. J. (2018).
 366 Diurnal variations in global Joule heating morphology and magnitude due

- 367 to neutral winds. *Journal of Geophysical Research: Space Physics*, *123*(3),
368 2398–2411.
- 369 Billett, D. D., Perry, G. W., Clausen, L. B. N., Archer, W. E., McWilliams,
370 K. A., Haaland, S., . . . Anderson, B. J. (2021). The Relationship Between
371 Large Scale Thermospheric Density Enhancements and the Spatial Distri-
372 bution of Poynting Flux. *Journal of Geophysical Research: Space Physics*,
373 e2021JA029205. doi: <https://doi.org/10.1029/2021JA029205>
- 374 Chisham, G., Lester, M., Milan, S. E., Freeman, M. P., Bristow, W. A., Grocott, A.,
375 . . . Walker, A. D. M. (2007). A decade of the Super Dual Auroral Radar Net-
376 work (SuperDARN): scientific achievements, new techniques and future direc-
377 tions. *Surveys in Geophysics*, *28*(1), 33-109. doi: 10.1007/s10712-007-9017-8
- 378 Cosgrove, R. B., Bahcivan, H., Chen, S., Strangeway, R. J., Ortega, J., Alhassan,
379 M., . . . others (2014). Empirical model of Poynting flux derived from FAST
380 data and a cusp signature. *Journal of Geophysical Research: Space Physics*,
381 *119*(1), 411–430.
- 382 Cowley, S. W. H., & Lockwood, M. (1992). Excitation and decay of solar wind-
383 driven flows in the magnetosphere-ionosphere system. In *Annales geophysicae*
384 (Vol. 10, pp. 103–115).
- 385 Coxon, J. C., Milan, S. E., Carter, J. A., Clausen, L. B. N., Anderson, B. J., & Ko-
386 rth, H. (2016). Seasonal and diurnal variations in AMPERE observations of
387 the Birkeland currents compared to modeled results. *Journal of Geophysical*
388 *Research: Space Physics*, *121*(5), 4027–4040.
- 389 Coxon, J. C., Shore, R. M., Freeman, M. P., Fear, R. C., Browett, S. D., Smith,
390 A. W., . . . Anderson, B. J. (2019). Timescales of Birkeland currents driven by
391 the IMF. *Geophysical Research Letters*, *46*(14), 7893–7901.
- 392 Deng, W., Killeen, T. L., Burns, A. G., & Roble, R. G. (1991). The flywheel ef-
393 fect: Ionospheric currents after a geomagnetic storm. *Geophysical research let-
394 ters*, *18*(10), 1845–1848.
- 395 Dods, J., Chapman, S. C., & Gjerloev, J. W. (2017). Characterizing the ionospheric
396 current pattern response to southward and northward IMF turnings with dy-
397 namical SuperMAG correlation networks. *Journal of Geophysical Research:
398 Space Physics*, *122*(2), 1883–1902.
- 399 Dungey, J. W. (1961). Interplanetary magnetic field and the auroral zones. *Physical*

- 400 *Review Letters*, 6(2), 47.
- 401 Greenwald, R. A., Baker, K. B., Dudeney, J. R., Pinnock, M., Jones, T. B., Thomas,
402 E. C., . . . others (1995). Darn/superdarn. *Space Science Reviews*, 71(1-4),
403 761–796.
- 404 Grocott, A., & Milan, S. E. (2014). The influence of IMF clock angle timescales
405 on the morphology of ionospheric convection. *Journal of Geophysical Research:*
406 *Space Physics*, 119(7), 5861–5876.
- 407 Iijima, T., Potemra, T. A., Zanetti, L. J., & Bythrow, P. F. (1984). Large-scale
408 Birkeland currents in the dayside polar region during strongly northward IMF:
409 A new Birkeland current system. *Journal of Geophysical Research: Space*
410 *Physics*, 89(A9), 7441–7452.
- 411 Knipp, D. J., Matsuo, T., Kilcommons, L., Richmond, A., Anderson, B., Korth, H.,
412 . . . Parrish, N. (2014). Comparison of magnetic perturbation data from LEO
413 satellite constellations: Statistics of DMSP and AMPERE. *Space Weather*,
414 12(1), 2–23.
- 415 Knipp, D. J., Richmond, A. D., Emery, B., Crooker, N. U., de La Beaujardiere, O.,
416 Evans, D., & Kroehl, H. (1991). Ionospheric convection response to changing
417 imf direction. *Geophysical research letters*, 18(4), 721–724.
- 418 Milan, S. E. (2009). Both solar wind-magnetosphere coupling and ring current
419 intensity control of the size of the auroral oval. *Geophysical Research Letters*,
420 36(18).
- 421 Milan, S. E., Carter, J. A., Sangha, H., Laundal, K. M., Østgaard, N., Tenfjord,
422 P., . . . others (2018). Timescales of dayside and nightside field-aligned cur-
423 rent response to changes in solar wind-magnetosphere coupling. *Journal of*
424 *Geophysical Research: Space Physics*, 123(9), 7307–7319.
- 425 Moretto, T., Hesse, M., Kuznetsova, M., Rastätter, L., Vennerstrøm, S., & Tenfjord,
426 P. (2021). How does the magnetosphere go to sleep? *Journal of Atmospheric*
427 *and Solar-Terrestrial Physics*, 105626.
- 428 Moretto, T., Hesse, M., Vennerstrøm, S., & Tenfjord, P. (2018). Estimating the rate
429 of cessation of magnetospheric activity in ampere field-aligned currents. *Geo-*
430 *physical Research Letters*, 45(23), 12–713.
- 431 Murr, D. L., & Hughes, W. J. (2001). Reconfiguration timescales of ionospheric con-
432 vection. *Geophysical Research Letters*, 28(11), 2145–2148.

- 433 Nishitani, N., Ruohoniemi, J. M., Lester, M., Benjamin, J., Baker, H., Koustov,
434 A. V., . . . Kikuchi, T. (2019). Review of the accomplishments of mid-latitude
435 Super Dual Auroral Radar Network (SuperDARN) HF radars. *Progress in*
436 *Earth and Planetary Science*, 6(1). doi: 10.1186/s40645-019-0270-5
- 437 Onsager, T. G., Scudder, J. D., Lockwood, M., & Russell, C. T. (2001). Recon-
438 nection at the high-latitude magnetopause during northward interplanetary
439 magnetic field conditions. *Journal of Geophysical Research: Space Physics*,
440 106(A11), 25467–25488.
- 441 Ruohoniemi, J. M., & Baker, K. B. (1998). Large-scale imaging of high-latitude con-
442 vection with Super Dual Auroral Radar Network HF radar observations. *Jour-*
443 *nal of Geophysical Research: Space Physics*, 103(A9), 20797–20811.
- 444 Shepherd, S. G. (2014). Altitude-adjusted corrected geomagnetic coordinates: Def-
445 inition and functional approximations. *Journal of Geophysical Research: Space*
446 *Physics*, 119(9), 7501–7521.
- 447 Snekvik, K., Østgaard, N., Tenfjord, P., Reistad, J. P., Laundal, K. M., Milan, S. E.,
448 & Haaland, S. E. (2017). Dayside and nightside magnetic field responses at
449 780 km altitude to dayside reconnection. *Journal of Geophysical Research:*
450 *Space Physics*, 122(2), 1670–1689.
- 451 Waters, C. L., Anderson, B. J., Greenwald, R. A., Barnes, R. J., & Ruohoniemi,
452 J. M. (2004). High-latitude poynting flux from combined Iridium and Super-
453 DARN data. In *Annales geophysicae* (Vol. 22, pp. 2861–2875).
- 454 Weimer, D. R. (2005). Improved ionospheric electrodynamic models and applica-
455 tion to calculating Joule heating rates. *Journal of Geophysical Research: Space*
456 *Physics*, 110(A5).
- 457 Yu, Y., & Ridley, A. J. (2009). Response of the magnetosphere-ionosphere system to
458 a sudden southward turning of interplanetary magnetic field. *Journal of Geo-*
459 *physical Research: Space Physics*, 114(A3).